ACS OMEGA

http://pubs.acs.org/journal/acsodf

Article

Research on Noise-Induced Characteristics of Unsteady Cavitation of a Jet Pump

Jian Gan, Kang Zhang, and Deming Wang*

Cite This: *ACS Omega* 2022, 7, 12255−12267

Read Online

ACCESS | Metrics & More | Article Recommendations | Supporting Information

ABSTRACT: The dynamic cavitation characteristics of normal-temperature water flowing through a transparent jet pump under different cavitation conditions were experimentally studied by adjusting the pressure ratio. The common results are presented at different pressure ratios, including the temporal and spatial changes of the pressure and noise, together with the visual observation of the cavitation unsteady behaviors using a high-speed camera. The analyses on the measured data and images reveal that the cavitation cloud is generated by periodic oscillations of the jet traveling pressure wave and the bubble traveling pressure wave. The oscillation of the two kinds of interface waves is caused by the collapse of the bubbles, which is the main mechanism of the bubble cloud shedding. As the pressure ratio increases, the maximum length of the jet cloud and bubble cloud linearly decreases, while their oscillation frequency increases gradually. Combined with the cavitation-cloud visualization data and noise frequency analysis, it is proposed that the strong impact between the jet traveling pressure wave and the bubble traveling pressure wave is the main cause of noise. Specially, the acoustic pressure reaches the maximum when the oscillation frequency of the jet traveling pressure wave is the same as that of the bubble traveling pressure wave. Also, the jet traveling pressure wave has a great influence on the migration of bubbles in the cavity. The results can provide guidance for the optimal operating condition in cavitation applications such as jet aerator and quantitative addition.

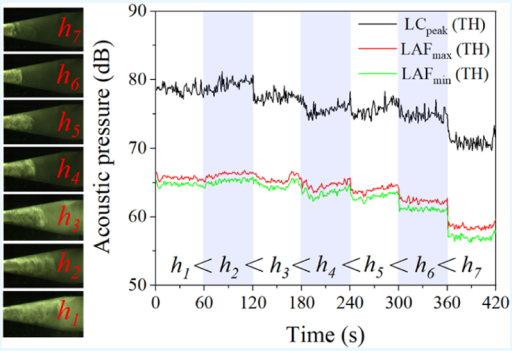

1. INTRODUCTION

Cavitation is of importance in various fields of engineering, including energy, shipbuilding, transportation, chemical industry, medicine, biology, aviation, aerospace, and other fields. In general, hydrodynamic cavitation can lead to many undesirable effects, such as noise, vibration, and material erosion,[1−3] and also results in local high temperature and pressure.[4,5] Due to the cavitation effects, hydrodynamic cavitation is widely used alone as an effective technique or in combination with other chemical, physical, and thermal techniques[6] in a large number of applications in the field of industrial dust removal and water treatment. With its mechanical and chemical effects, HC is successfully used for foam dust reduction,[7−10] quantitative addition of medicament,[9,11,12] sludge treatment,[13−17] water disinfection,[18,19] and alga removal.[20−22] Furthermore, it is also applied in the oxidation of organic pollutants in aqueous effluents.[23−26] Moreover, it has been already proven that HC can lead to a gradual disintegration of sludge suspended particles and also favors an increase of sludge solubilization.[13] However, hydrodynamic cavitation is extremely complicated and has not been fully understood, so it is necessary to carry out more research studies in order to better apply the cavitation effect to practice.

A jet pump is a common hydraulic machinery that is widely utilized in many fields such as in flow measurement, petrochemical industry, metallurgy, and other fields.[27] The jet pump is prone to cavitation due to its special internal structure. In the previous literature, a lot of research studies have been carried out on the cavitation mechanism of jet pumps, Venturi tubes, and other equipment. Knapp demonstrated the development of a liquid re-entrant jet for the first time. Brunhart et al.[28] have proven that there are two vapor-shedding mechanisms under cavitation conditions: re-entry flow and condensation shock through simulation and experiment. Long[29] reported that a liquid−vapor mixing shockwave is also observed under the operating-limit cavitation stage in jet pumps. Lu et al.[30] considered that there is a dynamic equilibrium interface wave between the bubble region and the liquid region when a jet pump produces cavitation. Also, the interface wave is the cause of pressure change. Zhu et al.[31] observed the upstream propagation of the shock wave-induced condensation front within the attached cavity in a variable pressure ratio wind tunnel and considered it to be the main

Received: February 2, 2022
Accepted: March 21, 2022
Published: April 1, 2022

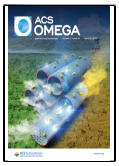

https://doi.org/10.1021/acsomega.2c00684
ACS Omega 2022, 7, 12255−12267

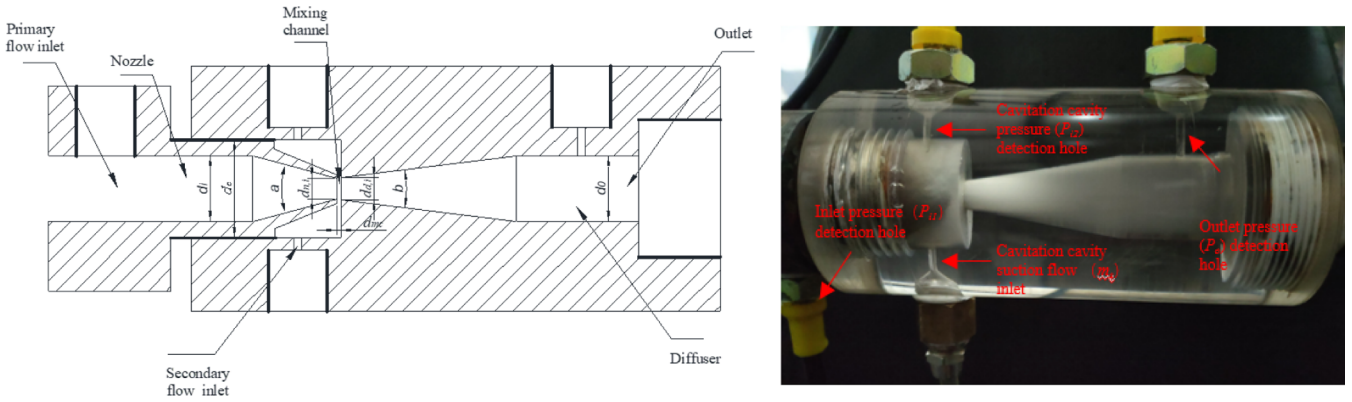

Figure 1. Schematic diagram of the internal structure of the cavitation jet device.

mechanism of cavitation shedding. Fang et al.[32] conducted a numerical study on the cavitation cloud shedding mechanism in a Venturi tube reactor by using a compressible cavitation phase-change solver and found that the main characteristic of the shedding mechanism induced by the re-entrant jet is the separation between the cavity and the wall. Jahangir[33] studied the performance of sheet cavitation and cloud cavitation and their main mechanisms in a Venturi system. The results showed that the re-entrant jet mechanism is the prevalent shedding mechanism at a large pressure ratio, while the shock wave mechanism is at a small pressure ratio. Far in the literature, many researchers tend to focus on the mechanism of cavitation shedding. Especially, the shedding mechanism caused by re-incident flow and bubbly shock waves has always been the focus of research and debate.[34] Generally, the sheet cavitation and cloud cavitation are more unstable with more obvious periodic shedding and collapse than choked cavitation. The choked cavitation dynamics are different from the sheet cavitation and cloud cavitation dynamics. Also, the pressure pulse, noise, and vibration caused by the jet pump are also different from those of the Venturi device due to the existence of the cavitation cavity. Therefore, more detailed research studies need to be done to probe the cavitation performance under the two mechanisms mentioned above and corresponding pressure pulsation and noise.

Generally, cavitation in the jet pump reactor can cause undesirable noise and vibration. If it is exposed to the environment for a long time, it will cause serious noise pollution and cause occupational diseases. However, for the jet aeration water treatment device, the large cavitation intensity can break the air into nanobubbles, which greatly increases the gas−liquid contact area and improves the mass transfer efficiency. Therefore, the increase of cavitation intensity is positive for the jet aerated-water treatment device. The cavitation intensity can be adjusted by the external flow parameters of the reactor and can be represented by noise and vibration from one aspect. Therefore, an in-depth understanding of the induced noise and vibration in various cavitation states not only helps to better control the undesired cavitation damage but also facilitates the operation of the jet aeration reactor. In the previous literature, Mancuso[35] conducted an experimental and numerical investigation on the performance of a swirling jet reactor with different geometric configurations and measured and analyzed the cavitation noise of different geometric shapes at different inlet pressures. Jablonská et al.[36] measured the noise intensity and vibration velocity of a spatialized Venturi tube with and without air saturation, respectively. The results indicated that the added air can suppress the noise intensity. Recently, Xu et al.[37] conducted an experimental study on the blocking cavitation performance and induced pressure pulsation, vibration, and noise of the Venturi reactor under different cavitation conditions. They consider that although the inlet pressure is different, the intensity of cavitation noise and vibration reaches the maximum under the same pressure ratio. These studies are of great significance to the noise and vibration characteristics caused by cavitation. However, there is no systematic study on the oscillation law of the reincident flow and shock wave produced by jet pump cavitation and the relationship between cavitation cloud oscillation and cavitation noise induction. Therefore, more experimental investigations are needed to study the unsteady cavitation dynamics of jet pumps.

In this paper, the experiments are conducted to study the oscillation law of cavitation clouds caused by unsteady cavitation of the jet pump and the source of cavitation noise by using a high-speed camera, high-frequency sensors, and an acoustic-level meter analyzer. Based on the instantaneous continuous cavitation visualization image, the PCC software was used to analyze the unsteady cavitation law of the jet pump to detect the jet cloud and bubble cloud oscillation mechanism, and the cavitation cloud oscillation law, noise induction law, and cavitation dynamics at different pressure ratios are connected. Through Fourier transform analysis of the collected data, the influence of two shedding mechanisms on noise is analyzed from the perspective of frequency resonance. The relationship between jet cavitation dynamics and cavitation noise can provide guidance for the optimal operation condition of the jet flow meters, jet aerators, and other devices.

2. CAVITATION THEORY OF THE JET PUMP

2.1. Theoretical Calculation of the Bubble Zone in the Jet Pump. Figure 1 illustrates the structure profile of the jet pump. When the water flow enters the contraction section of the jet pump, the flow velocity increases, and the kinetic energy increases due to the decrease of the cross-section. The kinetic energy reaches the maximum at the nozzle outlet. When the liquid flows out of the nozzle at high speed, negative pressure is formed at the nozzle outlet and the diffuser inlet.[38] Once the negative pressure decreases to the water vapor pressure, a very rapid partial transition from the liquid to gas phase occurs, and a liquid−gas two-phase flow forms. Despite the small value for the saturated water quantity, the volume of

https://doi.org/10.1021/acsomega.2c00684
ACS Omega 2022, 7, 12255−12267

producing bubbles is very large. However, the bubbles coalesce and break up gradually when they move downstream, where the pressure increases. The appearance form is the periodic oscillation of the bubble cloud and jet cloud.

The bubble quantity in the jet pump is largely dependent on the cavitation intensity. The cavitation intensity is affected by the outlet pressure when the inlet pressure is constant. Therefore, the ratio of the absolute pressure value between the outlet and the inlet of the jet pump is defined as the cavitation pressure ratio h, as shown in eq 1.

$$h = \frac{p_{o,abs}}{p_{i,abs}} \tag{1}$$

where $p_{i,abs}$ and $p_{o,abs}$ are the absolute static pressure at the inlet of the jet pump and the absolute static pressure at the outlet, respectively, and the subscripts abs represent the absolute pressure value.

2.2. Design of the Jet Pump. Assuming that the fluid flow in the convergent nozzle is one-dimensional isentropic flow, the relationship between static pressure and flow velocity can be easily calculated by using Bernoulli's equation between the jet pump inlet and nozzle outlet

$$p_i + \frac{1}{2}\rho_l v_i^2 + z_i = p_{n,o} + \frac{1}{2}\rho_l v_{n,o}^2 + K_1\frac{1}{2}\rho_l v_{n,o}^2 + z_{n,o} \tag{2}$$

where $z_i = z_{n,o}$, p_i and $p_{n,o}$ are the static pressures at the inlet and nozzle outlet of the jet pump, respectively, v_i and $v_{n,o}$ are the velocity at the jet pump inlet and nozzle outlet, respectively, on the axis, ρ_l is the working fluid, and K_1 is the energy loss coefficient of the contraction section. The value of this coefficient is affected by the shrinkage angle, wall surface roughness, and Reynolds number. When the working fluid flows through the shrink tube, $v_i \ll v_{n,o}$; if the energy loss of the shrink tube section is ignored, the mass flow rate of the working fluid can be approximately expressed as

$$m_w = \sqrt{\frac{1}{1+K_1}} \times \frac{\pi d_{n,o}^2}{4} \times \sqrt{2\rho_l} \times \sqrt{p_i - p_{n,o}} \tag{3}$$

where m_w is the mass flow of the working fluid and $d_{n,o}$ is the inner diameter of the nozzle outlet. In the cavitation state, the value of $p_{n,o}$ can be approximated to the saturated vapor pressure of water p_v, (p_v, =−97.7 kPa, 20 °C), so the relationship between the mass flow rate m_w and inlet pressure p_i can be written as

$$m_w = C_d \times \frac{\pi d_{n,o}^2}{4} \times \sqrt{2\rho_l} \times \sqrt{p_i - p_v} \tag{4}$$

where C_d is the flow compensation coefficient. In order to focus on the study of cavitation clouds in the diffuser, we designed a jet pump without a throat. Referring to previous studies,[39] we designed the specific parameters of the jet pump (see Table 1 for details) to achieve the minimum pressure loss of the jet pump.

3. EXPERIMENTAL RIG AND METHODS

3.1. Assembly of the Experimental System. The entire experimental system is shown in Figure 2. The system is mainly composed of a jet pump, liquid storage tank, liquid storage barrel, plunger pump, frequency conversion controller, regulating valve, high-speed camera, acoustic level meter analyzer, data acquisition system, and so forth. Table 2 shows the parameters of the experimental measuring instrument. The jet pump is composed of a nozzle and a diffuser. The nozzle is made of iron, and the cavitation cavity and diffuser are made of organic glass to facilitate visual observation of the cavitation process. Figure 1 shows the internal structure of the jet pump. Table 1 shows the internal structure parameters. The connecting pipeline of the system is the high-pressure hose with an inner diameter of 19 mm and a pressure resistance level of 10 MPa. U-shaped bolts are used for the connection between the pipelines. In order to ensure the tightness of the entire system, the butt joints of the high-pressure hose are sealed with O-rings. The O-ring is checked before the experiment to ensure its reliability. A raw material tape is used to seal the threaded connection part of the system. The pressure sensor and the flow meter are connected to the paperless recorder through a two-core communication cable and are connected to the computer through the RS485 to USB interface. After the connection is completed, the entire experimental system is debugged and run for 5 min under pressure, and the data monitoring situation is checked to ensure the normal operation of the experimental system.

Table 1. Jet Pump Structural Parameters

parameter	numerical value	remarks
d_i	16 mm	shrink tube entrance diameter
d_o	16 mm	diffusion tube outlet diameter
a	30 deg	convergent angle
b	14 deg	divergent angle
$d_{n,o}$	5 mm	the inner diameter of the jet pipe outlet
$d_{d,i}$	5.5 mm	diffusion tube inlet inner diameter
d_m	1.5 mm	mixing channel spacing
d_c	24 mm	cavitation cavity diameter

3.2. Experimental Operation Process. Before the test of the experimental system, the external water supply valve is opened to continuously supply water to ensure that there is sufficient water in the water tank and at the same time to ensure that the water temperature is constant. After the plunger pump is turned on, the system is kept running at low pressure (400−500 kPa) for 5 min to ensure that the air in the system is discharged. After the preparation work is completed, the outlet valve is kept in a fully open state. The inlet pressure of the jet pump is adjusted to a predetermined value by adjusting the frequency converter of the water pump. After the inlet pressure is stable, the outlet valve is closed from the fully open state and then slowly fully opened to obtain a suitable outlet pressure p_o so that the jet pump is in a different cavitation state. During the adjustment process, the process of initiation, development, and collapse of cavitation bubbles is carefully observed. The paperless recorder records the pressure and flow rate of each cavitation stage.

3.3. Data Collection Method. *3.3.1. Image Collection and Postprocessing Methods.* The high-speed camera model is PhantomVEO710L, which is saved in the high-fidelity video Cine format. Taking into account the resolution and sampling rate, two parameters are used to capture the cavitation state. The first setting resolution is 1280 × 720, and the shooting rate is 8300 fps. The second setting resolution is 1024 × 512, and the shooting rate is 14 000 fps. The macrolens model is Tokina AT-X PRO MACRO 100 F2.8 D. The camera is mounted on a tripod to eliminate vibration, and the LED nonstroboscopic fill light is used for illumination to obtain a

https://doi.org/10.1021/acsomega.2c00684
ACS Omega 2022, 7, 12255−12267

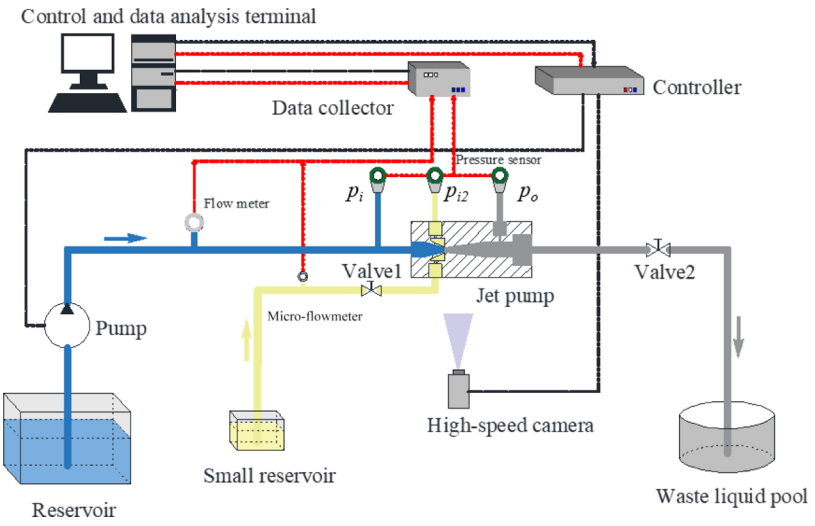

Figure 2. Schematic diagram of the experimental system.

Table 2. Experimental Measuring Instrument Parameters

apparatus	model	test range	precision (%)
data collector	BK-0896K		
flow meter 1 (Q_p)	LD-15	0.2−6 m^3/h	0.50
micro flow meter 2 (Q_s)	CX-M5.1	1−1000 mL/min	0.30
pressure sensor 1 (p_i)	BK-23XIM14	0−2.5 MPa	0.30
pressure sensor 2 (p_o)	BK-23XIM14	0−2.5 MPa	0.30
pressure sensor 3 (p_{i2})	BK-23XIM14	−0.1 to 0.3 MPa	0.30

clearer image. The cavitation image is captured in different cavitation states. The image captured by the high-speed camera is a sample for studying the state of cavitation. In order to ensure the reliability of the data, we need to collect more than 1000 pictures for each cavitation state, select 10 sets of data for each cavitation state amplitude, period, and frequency for processing, and take the average value.

PCC software is used for image postprocessing. For the collection of distance length, the scale is set and the scale calibration function of PCC is used to set the actual size corresponding to the reference scale in the picture (see Figure 3). PCC will automatically calculate the actual size represented by the unit pixel of the current picture and prompt that the calibration is complete. In this calibration process, we need to select different reference scales in the picture and calibrate 3−5 times. The one that most closely matches the actual size after calibration is selected as the basis for calculation. This method

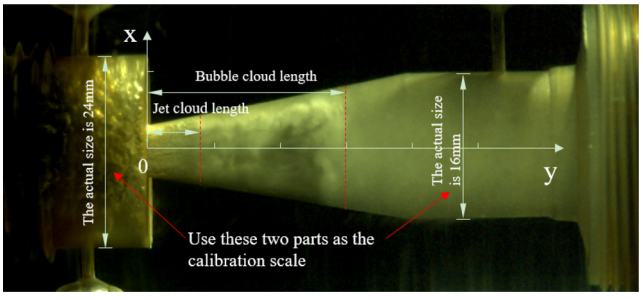

Figure 3. Calibration and collection of the jet cloud and bubble cloud length.

greatly improves the measurement accuracy and data collection efficiency.

3.3.2. Noise Collection. The SVAN971 new acoustic level meter analyzer was used to collect the acoustic pressure of each cavitation state. In order to reduce the impact of environmental noise on the measurement results, the experiment was carried out in a relatively open space. The closest distance between the reflector and the measured acoustic source was ensured to be at least twice the maximum distance from the microphone to the measured acoustic source. The height of the jet pump measured from the ground was 80 cm. For each cavitation state, the jet pump produced steady-state noise. When performing octave or 1/3 octave frequency band measurement, the shortest measurement period was 30 s for the frequency band with a center frequency of 160 Hz and below. For frequency bands with a center frequency of 200 Hz and above, the shortest measurement period was 10 s. In order to ensure the accuracy of data collection, our measurement time was 60 s. The results of the measurement period of 4 and 1 s were selected for Pearson correlation analysis. As shown in Figure 4, a two-tailed significance test was applied. The Pearson correlation coefficient was 0.99185, and the correlation was significant at the 0.05 level. Therefore, the results of these two measurement methods are consistent and reliable.

The *A*-weighted acoustic pressure level of the background noise (including wind noise at the microphone position) measured at the noise collection location is at least 10 dB lower than the acoustic pressure level emitted by the measured acoustic source without back-noise correction in order to achieve level 1 measurement accuracy. The difference between the measured background noise and the measured noise is much greater than 10 dB, so the measurement accuracy meets the level 1 accuracy condition.

The new SVAN971 acoustic level meter analyzer is a class 1 acoustic level meter. Inserting the microphone calibrator will automatically start the calibration process. In noise measurement, the measurement period T is composed of a series of submeasurement periods T_i, and each submeasurement period corresponds to a specified operating period of the acoustic source. In this case, it can usually be described by a single-emission acoustic pressure level L_p, which can be obtained by

https://doi.org/10.1021/acsomega.2c00684
ACS Omega 2022, 7, 12255−12267

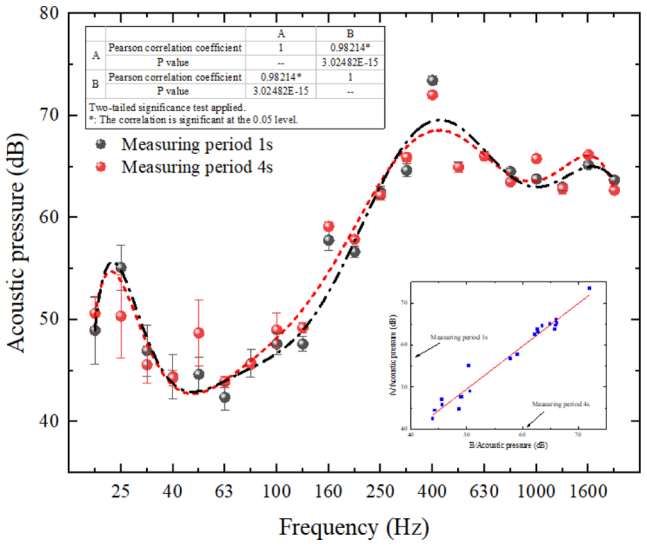

Figure 4. Pearson correlation analysis at different noise sampling periods.

energy-averaging the average emission acoustic pressure level of each submeasurement period according to eq 5

$$L_p = 10 \lg\left[\frac{1}{T}\sum_{i=1}^{N} T_i 10^{0.1L_{(p,T_i)}}\right] \quad (5)$$

$$T = \sum_{i=1}^{N} T_i \quad (6)$$

where T is the total measurement period, the unit is second; T_i is the i-th submeasurement period; N is the total number of submeasurement periods or operating periods; and $L_{(p,T_i)}$ is the A-weighted or frequency band emission acoustic in the submeasurement period T_i pressure, the unit is decibel.

Taking 4 s as the sampling period and a 60 s sampling duration, the acoustic pressures at different critical pressure ratios when the inlet pressure p_i = 700, 900, and 1100 kPa are measured. After each adjustment of the outlet pressure, it is necessary to wait for the water flow to stabilize for 2 min before measurement. According to experimental measurement, when the pressure ratio h > 0.6, the difference between the jet pump noise acoustic pressure and the background noise is less than 10 dB, and the measurement accuracy is lower than level 1. Therefore, this part of the data is not used for analysis.

4. RESULTS AND DISCUSSION

4.1. Visual Analysis of Cavitation. As shown in Figure 2, valve 1 is kept in the closed state, the secondary mass flow is Q_s = 0, and the outlet pressure is controlled by adjusting valve 2. The jet cavitation image is captured using a high-speed camera, and the resolution and sample rate of this process adopt the first setting. The bubble cloud shown in Figure 5 appears in the form of shadows. The darker the color, the greater the proportion of the gas phase, and the gas−liquid interface is more obvious during the oscillation process. During the cavitation and collapse of the cavitation cloud, a light−dark transition zone is produced. This is caused by the discontinuity of jet cavitation collapse.

As shown in Figure 5, the cavitation cloud has two interfaces that oscillate back and forth along the jet direction. The interface closer to the jet inlet is the interface between the jet cloud and the cavitation cloud (see the red dotted line in Figure 5), which we call the jet traveling pressure wave (predecessors called pressure traveling waves). This interface gradually moves upstream of the jet with the increase of the critical pressure ratio, and the fluctuation range is gradually reduced. Alos, when the critical pressure ratio in this state is

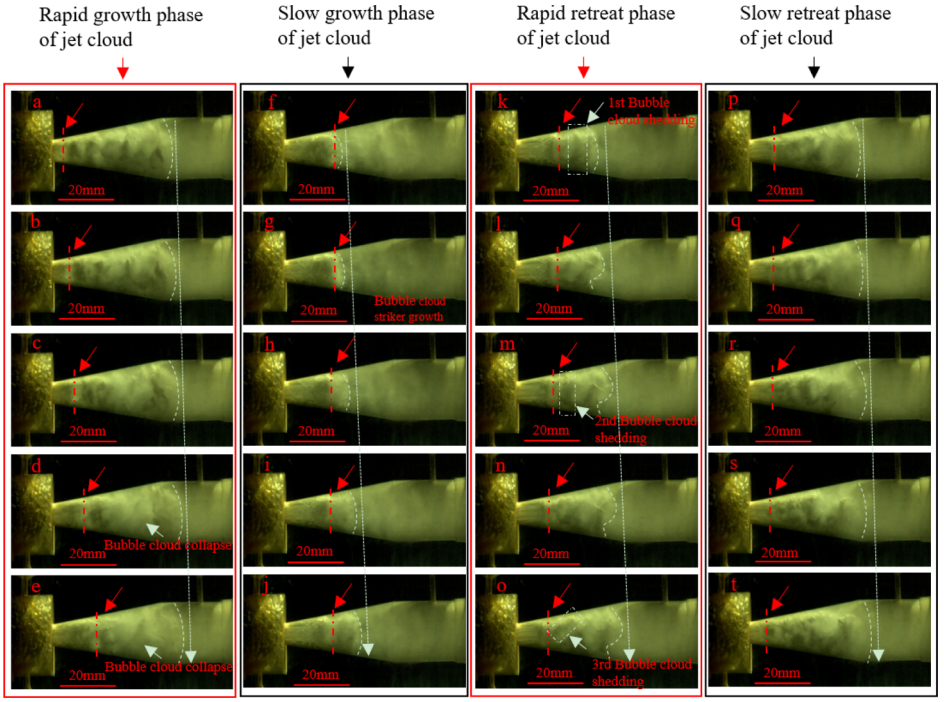

Figure 5. Oscillating law of jet clouds and the shedding of bubble clouds. Rapid growth phase of a jet cloud: (a−e). Slow growth phase of a jet cloud: (f−j). Rapid retreat phase of a jet cloud: (k−o). Slow retreat phase of a jet cloud: (p−t) (p_i = 900 kPa, p_o = 200 kPa, and Q_s = 0).

https://doi.org/10.1021/acsomega.2c00684
ACS Omega 2022, 7, 12255−12267

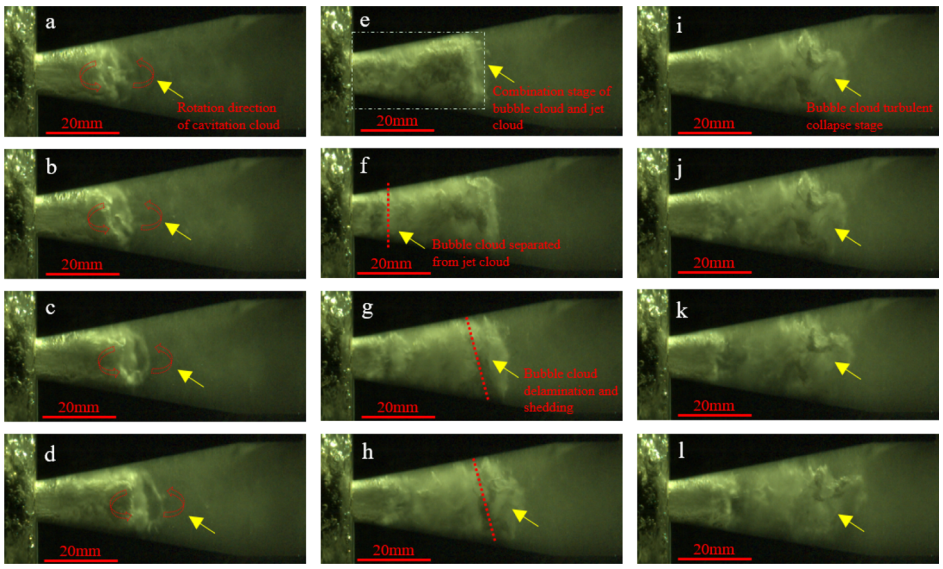

Figure 6. Growth and shedding of cavitation cloud vortices. Growth of cavitation cloud vortices: (a–e). Shedding of cavitation cloud vortices: (f–l) (p_i = 700 kPa, p_o = 168 kPa, and Q_s = 0).

reached, the interface disappears. Farther from the jet inlet is the interface between the bubble cloud and the liquid phase (see the white dotted line in Figure 5), which we call the bubble traveling pressure wave. The oscillation cycle of jet clouds can be divided into four stages: rapid growth, slow growth, rapid retreat, and slow retreat. Figure 5a–e in the red rectangle shows the rapid growth of the jet cloud. At this time, the bubble cloud is at the end of its growth, and the shadow of the bubble is lighter, indicating that this process is accompanied by the large-scale collapse of the bubble cloud. Figure 5f–j in the black rectangle shows the slow growth process of the jet cloud length before reaching the maximum. At this time, the bubble clouds of the previous stage completely collapsed, and the bubble clouds of the new stage gradually separated from the jet clouds and began to regenerate, starting a new round of oscillation cycle. Figure 5k–o in the red rectangle shows the rapid retreat of the jet cloud. Affected by the expansion of the jet clouds in the previous stage, the bubble clouds began to grow rapidly. The light and dark shaded area inside the cavitation cloud indicates that the cavitation cloud is beginning to stratify and fall off, as shown in the white dashed box in Figure 5. Figure 5p–t in the black rectangle shows the slow receding process of the jet cloud. At this stage, the bubble cloud reaches the maximum length and the shadow of the front peak of the bubble cloud becomes lighter, indicating that the bubble in the vanguard of the bubble cloud begins to collapse. The above analysis shows that the jet cloud and bubble cloud are always in a coupled oscillation state, and the jet cloud plays a leading role.

Figure 5 shows that the interface between the jet cloud and the bubble cloud is in a relatively clear vertical state, while the interface between the bubble clouds and the liquid phase is in the shape of a circular arc. This is due to the large velocity in the center of the jet, which causes the bubble cloud to spread rapidly, while the bubble cloud near the wall lags due to the influence of wall friction, adhesion, and turbulence. An irregular interface appears in Figure 5l–o in the red rectangular box, which is a common phenomenon of bubble cloud front collapse.

Figure 6a–d shows the rotational dynamic growth process of the cavitation cloud. The vortex state of the cavitation cloud often appears after the bubble cloud collapses in a large area. At this time, the jet cloud extends along the circumference of the diffuser and enters the expansion section at different axial jet velocities. The area near the wall of the diffuser with high jet velocity has a higher bubble density, which then forms a local pressure difference. When the jet enters the diffuser, its pressure immediately drops below the saturated vapor pressure of water, forming a cavitation cloud. The cavitation cloud grows in a vortex along the direction of the wall, forming a cavitation vortex cloud around the central axis. Figure 6e shows the transition stage of the turbulent combination of jet clouds and bubble clouds. At this stage, the jet cloud and the bubble cloud are mixed as a whole, and there is no obvious interface. Figure 6f–h shows the detachment process of the cavitation cloud and the jet cloud. During this process, the bubble cloud increases gradually and separates from the jet cloud until it collapses in disorder, as shown in Figure 6i–l.

In order to capture the initial cavitation state, it is necessary to adjust the outlet valve to close slowly so that the jet pump is in the critical cavitation state. The pressure ratio corresponding to this initial cavitation state is 0.77, and p_i = 52.5 kPa. When initial cavitation occurs, the bubbles are generated along the entrance circumference of the diffuser. Figure 7 shows that bubbles are intermittently generated in different parts of the diffuser. Especially, bubbles appear in different parts of the diffusion tube at the same time, as shown in Figure 7f. From

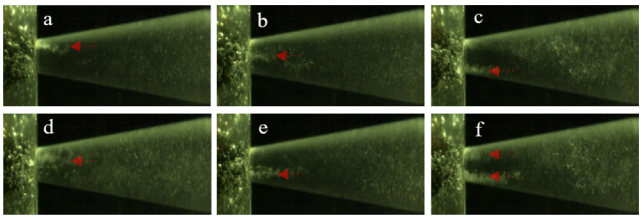

Figure 7. Initial cavitation state in different parts of the diffuser inlet: (a–f).

https://doi.org/10.1021/acsomega.2c00684
ACS Omega 2022, 7, 12255–12267

the analysis of the above phenomenon, it can be seen that the generation of initial cavitation bubbles is random. Also, this is because the shear flow at the inlet of the diffuser promotes the intermittent generation of bubbles.

Figure 8 shows the state of bubbles in the cavitation cavity of the jet pump at different pressure ratios. As the pressure ratio

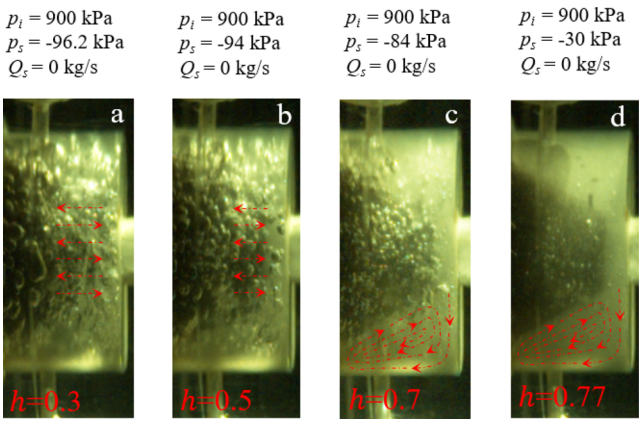

Figure 8. Law of bubble movement in the cavitation cavity of the jet pump. (The pressure ratio of (a–d) is 0.3, 0.5, 0.7, and 0.77, respectively.)

of the bubbles in the cavitation cavity increases, the bubble density and bubble diameter decrease gradually. As shown in Figure 8a,b, when the pressure ratio $h < 0.58$, affected by the oscillation of the jet cloud, the movement of the bubbles oscillates periodically in the direction of the jet, and the amplitude decreases as the pressure ratio increases. As shown in Figure 8c,d, when the pressure ratio $h > 0.58$, the periodic oscillation of the jet cloud disappears. The trajectory of the movement of the bubbles in the cavity is affected by the shear flow generated by the steady-state jet, and the circular flow is formed along the inner wall of the cavitation cavity, which rotates in a vortex shape. In the video taken using a high-speed camera, it can be observed that when the pressure ratio $h < 0.58$, the bubbles expand and contract periodically under the influence of the jet cloud oscillation. In the gap between the jet outlet and the diffuser inlet, the bubble initiation phenomenon caused by the shear flow can be observed. The newly born bubbles enter the cavitation cavity with the oscillation of the jet cloud, and there also occur the phenomena of merging and splitting of bubbles at the same time. The above analysis shows that the oscillation intensity in the cavitation cavity can be adjusted by controlling the pressure ratio, which can be used to improve the premixing effect of the quantitative adding device, such as the fixed ratio addition of the surfactant in coal mine foam dust reduction.

4.2. Analysis of Cavitation Cloud Oscillation. As shown in Figure 9, 0–300 s of the *X*-axis is the decreasing stage of outlet pressure, and 300–600 s of the *X*-axis is the increasing stage of outlet pressure. In order to improve the identifiability of the maximum length of the bubble cloud, the inlet pressure p_i is set to 1100 kPa and the secondary flow valve is kept closed. When p_o gradually decreases, the change in the suction negative pressure can be divided into two stages: linear rapid increase and nonlinear slow increase with p_o = 620 kPa as the dividing point. When the outlet pressure gradually increases, the demarcation point appears at p_o = 696 kPa. The cavitation time lag is obvious.

When the outlet pressure p_o gradually decreases, the change of the bubble cloud length can be divided into two stages: linear increase and constant state with p_o = 220 kPa as the demarcation point. When the outlet pressure gradually increases, this demarcation point appears at p_o = 252 kPa, and this demarcation point is also significantly higher than the process of reducing the outlet pressure. It can be seen that the boundary point appears at a relatively low pressure when the outlet pressure decreases, and the boundary point appears at a relatively high pressure when the outlet pressure increases. It shows that the maximum length of the bubble cloud has different sensitivity points to different outlet pressure adjustment processes. There is also a certain time lag in the length of the bubble clouds.

As shown in Figure 10, when p_i = 900 kPa, p_o = 180 kPa, and Q_s = 0, the oscillation period of the bubble cloud and jet cloud is basically consistent. The maximum length of the bubble cloud is significantly greater than the length of the jet cloud, and the minimum length of the bubble cloud appears before the maximum length of the jet cloud. The maximum length of

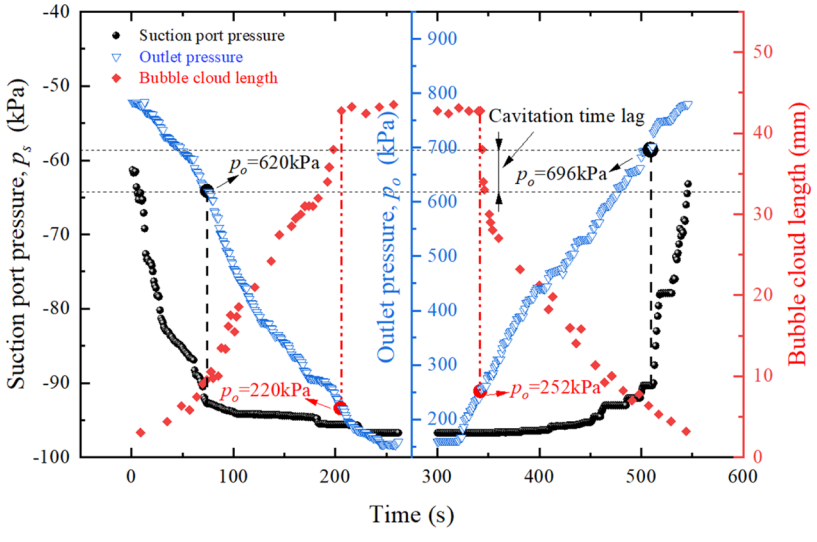

Figure 9. Variation of suction port pressure and cavitation cloud length with time (p_i = 1100 kPa and Q_s = 0).

https://doi.org/10.1021/acsomega.2c00684
ACS Omega 2022, 7, 12255–12267

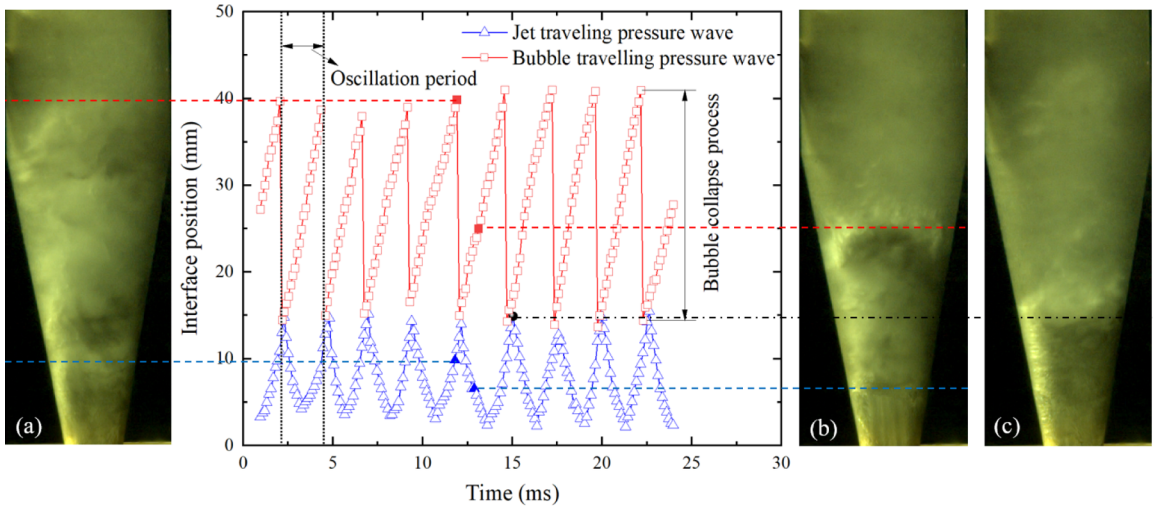

Figure 10. Variation of two kinds of interface positions with time. (a−c) Interface states of the jet traveling pressure wave and the bubble traveling pressure wave (p_i = 900 kPa, p_o = 180 kPa, and Q_s = 0).

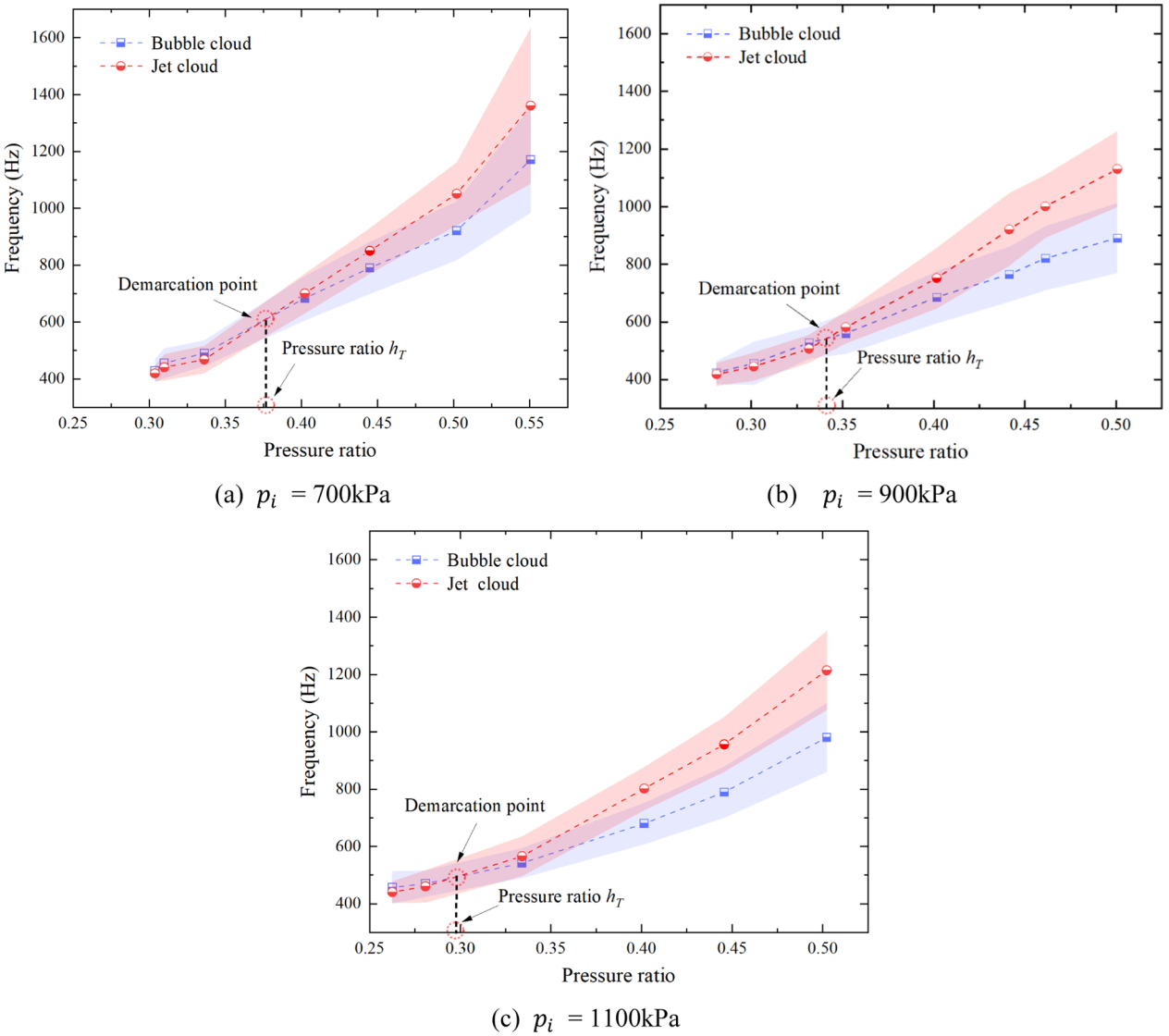

Figure 11. Oscillation frequency corresponding to the jet cloud and bubble cloud under different pressure ratios. The inlet pressures of (a−c) are 700, 900, and 1100 kPa, respectively.

https://doi.org/10.1021/acsomega.2c00684
ACS Omega 2022, 7, 12255−12267

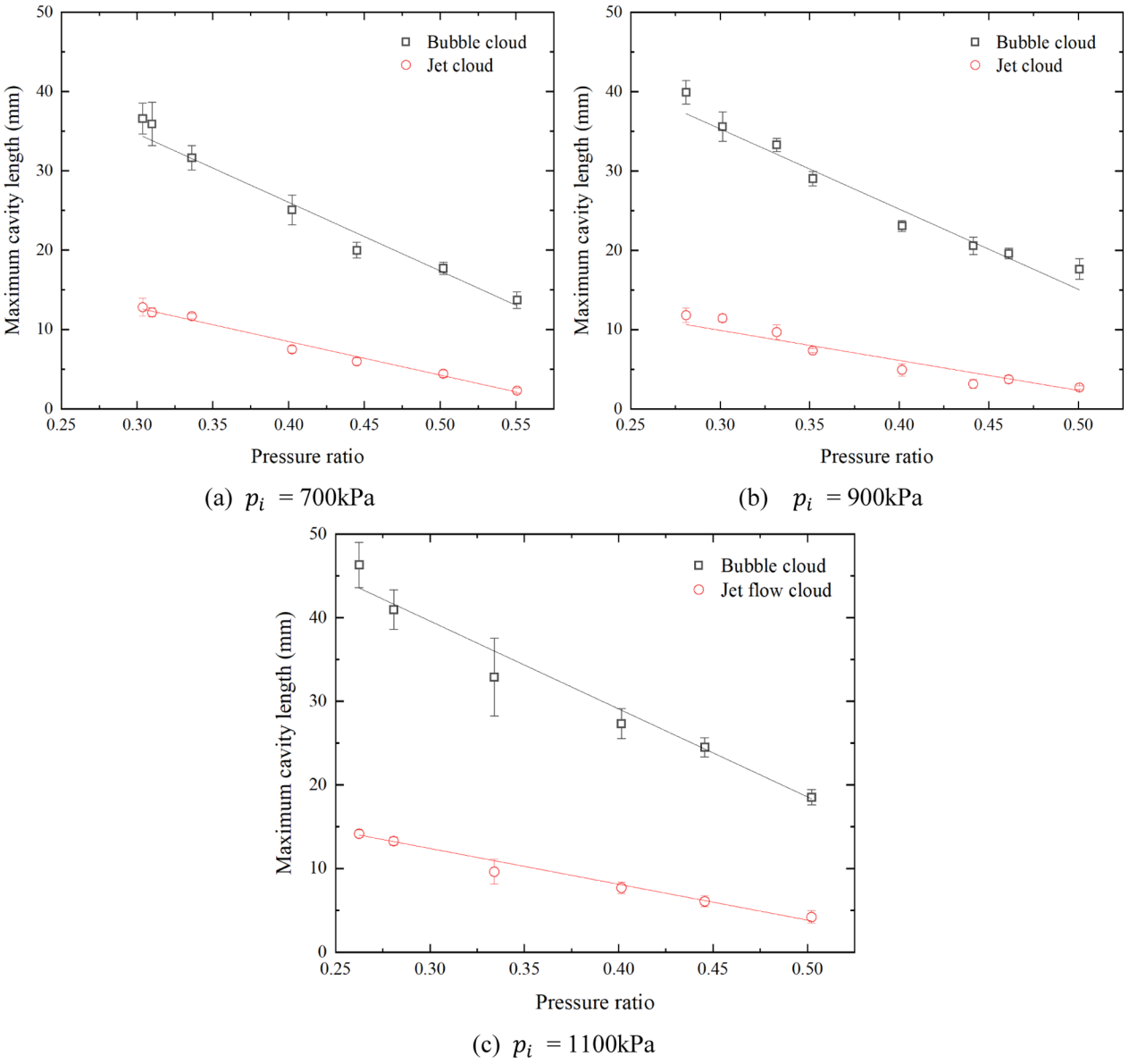

Figure 12. Variations of the maximum length of the jet cloud and bubble cloud with the pressure ratio. The inlet pressures of (a−c) are 700, 900, and 1100 kPa, respectively.

the bubble cloud appears after the minimum length of the jet cloud. As shown in Figure 10b, when the bubble traveling pressure wave grows rapidly, the jet traveling pressure wave decreases slowly. As shown in Figure 10a, when the interface of the bubble traveling pressure wave reaches the maximum, the jet traveling pressure wave still movesforward. Figure 10c shows the location of the intersection of the two interface waves after the bubbles collapse. Although there are inevitable errors in data acquisition, it is obvious that the bubble pressure traveling wave will fall back instantly after it reaches the maximum. Although there are inevitable errors in data collection, it can be clearly seen that after the bubble pressure traveling wave reaches the maximum, a cliff-like retreat will occur. Then, the two interface waves travel toward each other and collide. This phenomenon is caused by the large-scale collapse of bubbles.

As shown in Figure 11, the oscillation frequency of bubble cloud and jet cloud increases with the increase of pressure ratio. However, the growth rate of the jet cloud is greater than that of the bubble cloud, indicating that the jet cloud is more sensitive to the high pressure ratio. When the pressure ratio h = 0.5−0.55, the boundary between the jet cloud and the bubble cloud becomes blurred. Also, when the pressure ratio continues to increase, the jet cloud disappears. At the same time, as the pressure ratio increases, there is always a critical pressure ratio h_T that makes the oscillation frequency of the jet cloud and bubble cloud consistent. The value of this pressure ratio gradually decreases as the inlet pressure increases (as shown by the black dotted line in Figure 11). When $h = h_T$, the oscillation frequency of the jet cloud and bubble cloud resonates. We will discuss the relationship between this phenomenon and noise in Section 4.3. As shown in the red and blue areas in Figure 11, as the pressure ratio increases, the error range (standard deviation) of the oscillation frequency of the jet cloud and bubble cloud also increases. It shows that the cavitation cloud becomes unstable as the pressure ratio increases, and the boundary of the shock also becomes blurry.

https://doi.org/10.1021/acsomega.2c00684
ACS Omega 2022, 7, 12255−12267

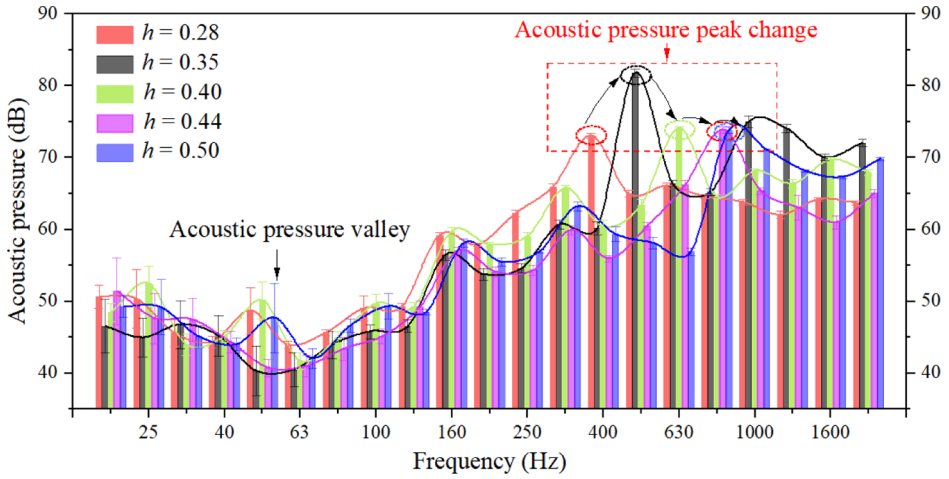

Figure 13. Variation of the acoustic pressure at different pressure ratios (p_i = 900 kPa and Q_s = 0).

As shown in Figure 12, the maximum oscillation length of the jet cloud and bubble cloud linearly decreases with the increase of pressure ratio. Comparing the slopes of the fitting curves, it can be seen that when the inlet pressure p_i = 1100 kPa, the slope of the fitting curve of the maximum bubble cloud length k_b = −105, and the slope of the fitting curve of the maximum jet cloud length k_j = −42.7. When p_i = 900 kPa, k_b = −101.1 and k_j = −39.9. When p_i = 700 kPa, k_b = −86.5 and k_j = −42.3. The results show that the slope of the fitting curve of the maximum length of bubble cloud tends to be smooth with the decrease of inlet pressure, while the slope of the fitting curve of the maximum jet cloud length is basically unchanged. This shows that the bubble cloud has a larger change with the change of the inlet pressure than the jet cloud (Figure 12).

4.3. Analysis of Cavitation Noise. In order to explore the relationship between jet clouds and bubble clouds and noise sources, we monitored the frequency of noise under different inlet pressures and at different pressure ratios. Figures 13 and 14 show the typical results obtained by the first Fourier transform.

As shown in Figure 13, the maximum acoustic pressure for different pressure ratios occurs between 400 and 1000 Hz, while the minimum acoustic pressure occurs between 40 and 50 Hz. As shown in the red dotted frame in Figure 13, the maximum acoustic pressure first increases and then decreases with the increase of the pressure ratio, which is also verified by Figures S1 and S3 in the Supporting Information file. When p_i = 900 kPa and h = 0.35, the acoustic pressure of the noise reaches the maximum of 81.7 dB. Therefore, the maximum acoustic pressure of cavitation noise can be reduced or increased by controlling the pressure ratio. For the quantitative dosing device, noise can cause damage to the hearing of the operator, and it is also a kind of energy loss, so it should be avoided as much as possible. However, achieving the maximum vibration intensity is desirable for water treatment processes, such as alga removal that requires a higher vibration intensity.

Figure 14 compares the relationship between the acoustic frequency corresponding to the maximum acoustic pressure and the bubble cloud oscillation frequency at different pressure ratios. The red and blue shaded areas are the error (standard deviation) range of the cavitation cloud oscillation frequency. When p_i = 900 kPa and h = 0.28, the oscillation frequency of the jet cloud is slightly lower than that of the bubble cloud. The maximum acoustic pressure appears in the frequency range covered by the jet cloud and bubble cloud. As shown in Figure 14a−e, the noise frequency corresponding to the maximum acoustic pressure value is always within the frequency range of bubble cloud oscillation. When h = 0.4 and 0.5, the area covered by the oscillation frequency of the bubble cloud and jet cloud gradually separates. When h = 0.5, the maximum acoustic pressure only appears in the red shaded area covered by the oscillation frequency of the bubble cloud. The above analysis shows that the oscillation frequency of the bubble cloud is closely related to the noise generation.

In particular, as shown in Figures S1 and S3 in the Supporting Information file, the pressure ratio corresponding to the maximum acoustic pressure varies with different inlet pressures, which is contrary to the experimental conclusion of Venturi with throat by Xu et al.[37] Since two kinds of traveling pressure waves with the same frequency have a synergistic enhancement effect on noise, we infer that this phenomenon is related to the resonance frequency of jet clouds and bubble clouds. The conditions for the appearance of the maximum acoustic pressure value under different inlet pressures are (1) p_i = 700 and h = 0.40; (2) p_i = 900 and h = 0.35; (3) p_i = 1100 and h = 0.33. When the inlet pressure increases, the pressure ratio corresponding to the maximum acoustic pressure decreases, which is consistent with the law of pressure ratio h_T corresponding to the resonance frequency mentioned in Section 4.2. As shown in Figure 11, when p_i = 700, 900, and 1100 kPa, h_T is approximately 0.38, 0.34, and 0.29, respectively. Although h_T is a predicted value with error, the critical pressure ratio corresponding to the maximum acoustic pressure is basically the same. Therefore, the conclusion is reliable.

Combined with the analysis in Sections 4.1 and 4.2, we give the following explanation for the generation of noise: as shown in Figures 5 and 10, the collapse of the bubble clouds causes the interface between the bubble cloud and the liquid phase to retreat rapidly. At this time, the jet traveling pressure wave and the bubble traveling pressure wave move toward each other quickly and hedge. The high-frequency and high-intensity impact force strikes the inner wall of the diffusion tube, resulting in intermittent noise. Because of the high frequency of impact, the human ear cannot distinguish. The generation of cavitation noise is somewhat similar to the water hammer effect. In short, the impact of the jet traveling pressure wave and the bubble traveling pressure wave produces noise, and the

https://doi.org/10.1021/acsomega.2c00684
ACS Omega 2022, 7, 12255−12267

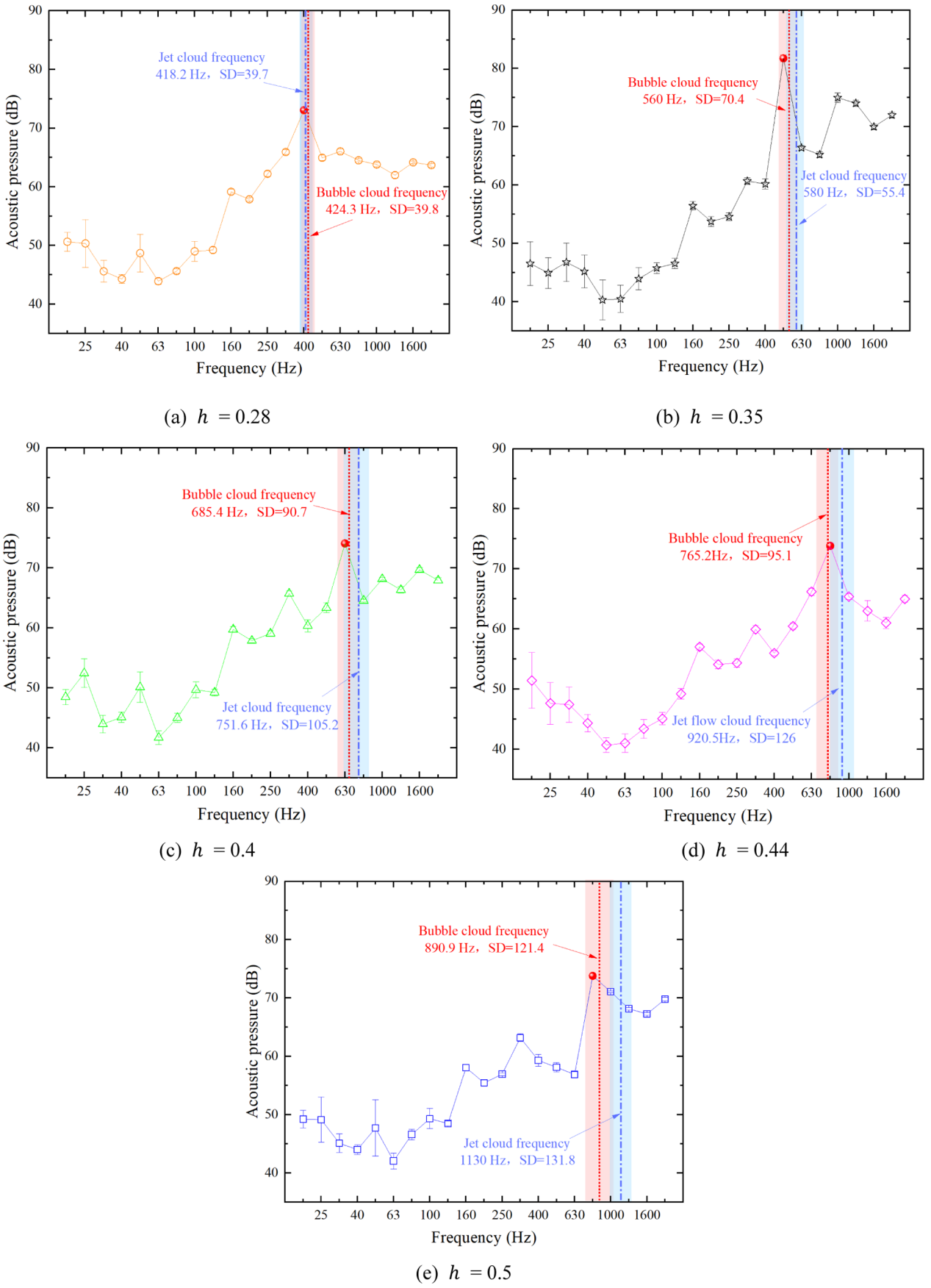

Figure 14. Relationship between the oscillation frequency of the cavitation cloud and the acoustic pressure of cavitation noise. The pressure ratios of (a−e) are 0.28, 0.35, 0.4, 0.44, and 0.5, respectively (p_i = 900 kPa and Q_s = 0).

https://doi.org/10.1021/acsomega.2c00684
ACS Omega 2022, 7, 12255−12267

frequency of the bubble traveling pressure wave determines the frequency of the maximum acoustic pressure.

5. CONCLUSIONS

In this paper, the oscillating law of the bubble cloud and jet cloud of the jet pump is studied experimentally, and the cause of cavitation noise is deeply studied. The main conclusions are as follows:

(1) High-speed video image sequences illustrate that the jet cloud plays a leading role in the oscillation state. Also, the vortex growth of bubble clouds is considered to be a common phenomenon, which is related to the different jet velocities on the wall of the diffusion tube. When the pressure ratio $h < 0.58$, the bubble in the cavitation cavity oscillates with the oscillation of the traveling pressure wave. When the pressure ratio $h > 0.58$, the jet cloud disappears and the bubble forms a circulation along the inner wall of the cavitation cavity. In the initial cavitation stage, the generation of bubbles around the inlet of the diffusion tube is intermittent, random, and asymmetric. Also, the shear flow with different velocities at the entrance of the diffusion tube is considered to be the main reason. These observations explain the ability for the regularity of the process, irrespective of the complex flow fields which can be found downstream of the diffusion tube.

(2) The normal periodic oscillation state of the two traveling pressure waves is that they collide with each other and then move in opposite directions. There is a certain time lag when the maximum length of the bubble cloud varies with the outlet pressure. With the increase of pressure ratio, the length of the jet cloud and bubble cloud decreases linearly, while the oscillation frequency increases. There is always a critical pressure ratio h_T that makes the oscillation frequencies of jet cloud and bubble cloud the same. Also, h_T decreases with the increase of the inlet pressure p_i.

(3) When the inlet pressure is constant, the maximum acoustic pressure increases at first and then decreases with the increase of pressure ratio. The acoustic pressure reaches the maximum at h_T. The impact of the jet traveling pressure wave and the bubble traveling pressure wave is the main cause of the noise. Also, the frequency of the bubble traveling pressure wave determines the frequency of the maximum acoustic pressure.

■ ASSOCIATED CONTENT

Supporting Information

The Supporting Information is available free of charge at https://pubs.acs.org/doi/10.1021/acsomega.2c00684.

Acoustic pressure under different conditions (p_i = 700 kPa and Q_s = 0 and p_i = 1100 kPa and Q_s = 0) (PDF)

■ AUTHOR INFORMATION

Corresponding Author

Deming Wang − *Key Laboratory of Gas and Fire Control for Coal Mines, School of Safety Engineering, China University of Mining & Technology, Xuzhou 221116, China;* orcid.org/0000-0002-4324-9397; Email: dmwcumt@outlook.com

Authors

Jian Gan − *Key Laboratory of Gas and Fire Control for Coal Mines, School of Safety Engineering, China University of Mining & Technology, Xuzhou 221116, China*

Kang Zhang − *Key Laboratory of Gas and Fire Control for Coal Mines, School of Safety Engineering, China University of Mining & Technology, Xuzhou 221116, China*

Complete contact information is available at: https://pubs.acs.org/10.1021/acsomega.2c00684

Author Contributions

J.G.: investigation, data curation, and writing—original draft. K.Z.: investigation—review and editing. D.W.: conceptualization and methodology.

Notes

The authors declare no competing financial interest.

■ ACKNOWLEDGMENTS

This work was supported by the Key Program of the National Natural Science Foundation of China (grant no. 52130411) and the National Natural Science Foundation of China (grant no. 51974299).

■ REFERENCES

(1) Haosheng, C.; Jiang, L.; Darong, C.; Jiadao, W. Damages on steel surface at the incubation stage of the vibration cavitation erosion in water. *Wear* **2008**, *265*, 692−698.

(2) Dular, M. Hydrodynamic cavitation damage in water at elevated temperatures. *Wear* **2016**, *346*−*347*, 78−86.

(3) Hutli, E.; Nedeljkovic, M. S.; Radovic, N. A.; Bonyár, A. The relation between the high speed submerged cavitating jet behaviour and the cavitation erosion process. *Int. J. Multiphase Flow* **2016**, *83*, 27−38.

(4) Pathania, S.; Ho, Q. T.; Hogan, S. A.; McCarthy, N.; Tobin, J. T. Applications of hydrodynamic cavitation for instant rehydration of high protein milk powders. *J. Food Eng.* **2018**, *225*, 18−25.

(5) Yi, C.; Lu, Q.; Wang, Y.; Wang, Y.; Yang, B. Degradation of organic wastewater by hydrodynamic cavitation combined with acoustic cavitation. *Ultrason. Sonochem.* **2018**, *43*, 156−165.

(6) Mancuso, G.; Langone, M.; Andreottola, G.; Bruni, L. Effects of hydrodynamic cavitation, low-level thermal and low-level alkaline pretreatments on sludge solubilisation. *Ultrason. Sonochem.* **2019**, *59*, 104750.

(7) Lu, X.; Wang, D.; Xu, C.; Zhu, C.; Shen, W. Experimental investigation and field application of foam used for suppressing roadheader cutting hard rock in underground tunneling. *Tunn. Undergr. Space Technol.* **2015**, *49*, 1−8.

(8) Lu, X.-x.; Wang, D.-m.; Zhu, C.-b.; Shen, W.; Zhong, X.-x.; Xu, C.-h. A new adding method of foaming agent used for foam dust suppression in underground coal mines. *J. Cent. South Univ.* **2015**, *22*, 3116−3122.

(9) Wang, Q.; Wang, D.; Wang, H.; Shen, Y.; Zhu, X. Experimental investigations of a new surfactant adding device used for mine dust control. *Powder Technol.* **2018**, *327*, 303−309.

(10) Wang, Q.; Wang, D.; Wang, H.; Han, F.; Zhu, X.; Tang, Y.; Si, W. Optimization and implementation of a foam system to suppress dust in coal mine excavation face. *Process Saf. Environ. Prot.* **2015**, *96*, 184−190.

(11) Zhu, X.; Wang, D.; Wang, H.; Zhu, Y.; Xu, C. A cavitating device for mini quantitative liquid addition. *Flow Meas. Instrum.* **2017**, *57*, 87−93.

(12) Zhu, X.; Wang, D.; Xu, C.; Zhu, Y.; Zhou, W.; He, F. Structure influence on jet pump operating limits. *Chem. Eng. Sci.* **2018**, *192*, 143−160.

(13) Mancuso, G.; Langone, M.; Di Maggio, R.; Toscano, A.; Andreottola, G. Effect of hydrodynamic cavitation on flocs structure

in sewage sludge to increase stabilization for efficient and safe reuse in agriculture. *Biorem. J.* **2022**, *26*, 41−52.
(14) Lee, G.; Lee, I.; Han, J.-I. A combined method of hydrodynamic cavitation and alkaline treatment for waste-activated sludge solubilization; N/P recovery from anaerobic granular sludge. *J. Environ. Chem. Eng.* **2019**, *7*, 103329.
(15) Mancuso, G.; Langone, M.; Andreottola, G. A swirling jet-induced cavitation to increase activated sludge solubilisation and aerobic sludge biodegradability. *Ultrason. Sonochem.* **2017**, *35*, 489−501.
(16) Bhat, A. P.; Gogate, P. R. Cavitation-based pre-treatment of wastewater and waste sludge for improvement in the performance of biological processes: A review. *J. Environ. Chem. Eng.* **2021**, *9*, 104743.
(17) Jung, K.-W.; Hwang, M.-J.; Yun, Y.-M.; Cha, M.-J.; Ahn, K.-H. Development of a novel electric field-assisted modified hydrodynamic cavitation system for disintegration of waste activated sludge. *Ultrason. Sonochem.* **2014**, *21*, 1635−1640.
(18) Mancuso, G.; Langone, M.; Andreottola, G. A critical review of the current technologies in wastewater treatment plants by using hydrodynamic cavitation process: principles and applications. *J. Environ. Health Sci. Eng.* **2020**, *18*, 311−333.
(19) Mancuso, G.; Langone, M.; Andreottola, G.; Bruni, L. Effects of hydrodynamic cavitation, low-level thermal and low-level alkaline pre-treatments on sludge solubilisation. *Ultrason. Sonochem.* **2019**, *59*, 104750.
(20) Wu, Z.; Shen, H.; Ondruschka, B.; Zhang, Y.; Wang, W.; Bremner, D. H. Removal of blue-green algae using the hybrid method of hydrodynamic cavitation and ozonation. *J. Hazard. Mater.* **2012**, *235−236*, 152−158.
(21) Li, P.; Song, Y.; Yu, S. Removal of Microcystis aeruginosa using hydrodynamic cavitation: Performance and mechanisms. *Water Res.* **2014**, *62*, 241−248.
(22) Batista, M. D.; Anhê, A. C. B. M.; de Souza Inácio Gonçalves, J. C. Use of Hydrodynamic Cavitation for Algae Removal: Effect on the Inactivation of Microalgae Belonging to Genus Scenedesmus. *Water, Air, Soil Pollut.* **2017**, *228*, 443.
(23) Mancuso, G.; Langone, M.; Laezza, M.; Andreottola, G. Decolourization of Rhodamine B: A swirling jet-induced cavitation combined with NaOCl. *Ultrason. Sonochem.* **2016**, *32*, 18−30.
(24) Capocelli, M.; De Crescenzo, C.; Karatza, D.; Lancia, A.; Musmarra, D.; Piemonte, V.; Prisciandaro, M. A Transport-Phenomena Approach to Model Hydrodynamic Cavitation of Organic Pollutants. *Water* **2020**, *12*, 1564.
(25) Gągol, M.; Cako, E.; Fedorov, K.; Soltani, R. D. C.; Przyjazny, A.; Boczkaj, G. Hydrodynamic cavitation based advanced oxidation processes: Studies on specific effects of inorganic acids on the degradation effectiveness of organic pollutants. *J. Mol. Liq.* **2020**, *307*, 113002.
(26) Badmus, K. O.; Tijani, J. O.; Massima, E.; Petrik, L. Treatment of persistent organic pollutants in wastewater using hydrodynamic cavitation in synergy with advanced oxidation process. *Environ. Sci. Pollut. Res.* **2018**, *25*, 7299−7314.
(27) Soyama, H.; Hoshino, J. Enhancing the aggressive intensity of hydrodynamic cavitation through a Venturi tube by increasing the pressure in the region where the bubbles collapse. *AIP Adv.* **2016**, *6*, 045113.
(28) Brunhart, M.; Soteriou, C.; Gavaises, M.; Karathanassis, I.; Koukouvinis, P.; Jahangir, S.; Poelma, C. Investigation of cavitation and vapor shedding mechanisms in a Venturi nozzle. *Phys. Fluids* **2020**, *32*, 083306.
(29) Long, X.; Yao, H.; Zhao, J. Investigation on mechanism of critical cavitating flow in liquid jet pumps under operating limits. *Int. J. Heat Mass Transfer* **2009**, *52*, 2415−2420.
(30) Lu, X.; Wang, D.; Shen, W.; Zhu, C. Experimental investigation of the propagation characteristics of an interface wave in a jet pump under cavitation condition. *Exp. Therm. Fluid Sci.* **2015**, *63*, 74−83.
(31) Zhu, J.; Xie, H.; Feng, K.; Zhang, X.; Si, M. Unsteady cavitation characteristics of liquid nitrogen flows through venturi tube. *Int. J. Heat Mass Transfer* **2017**, *112*, 544−552.
(32) Fang, L.; Li, W.; Li, Q.; Wang, Z. Numerical investigation of the cavity shedding mechanism in a Venturi reactor. *Int. J. Heat Mass Transfer* **2020**, *156*, 119835.
(33) Jahangir, S.; Hogendoorn, W.; Poelma, C. Dynamics of partial cavitation in an axisymmetric converging-diverging nozzle. *Int. J. Multiphase Flow* **2018**, *106*, 34−45.
(34) Wang, C.; Huang, B.; Wang, G.; Zhang, M.; Ding, N. Unsteady pressure fluctuation characteristics in the process of breakup and shedding of sheet/cloud cavitation. *Int. J. Heat Mass Transfer* **2017**, *114*, 769−785.
(35) Mancuso, G. Experimental and numerical investigation on performance of a swirling jet reactor. *Ultrason. Sonochem.* **2018**, *49*, 241−248.
(36) Jablonská, J.; Mahdal, M.; Kozubková, M. Spectral Analysis of Pressure, Noise and Vibration Velocity Measurement in Cavitation. *Meas. Sci. Rev.* **2017**, *17*, 250−256.
(37) Xu, S.; Wang, J.; Cheng, H.; Ji, B.; Long, X. Experimental study of the cavitation noise and vibration induced by the choked flow in a Venturi reactor. *Ultrason. Sonochem.* **2020**, *67*, 105183.
(38) Lu, X.; Wang, D.; Shen, W.; Cao, K. A New Design of Double-Stage Parallel Adding Equipment Used for Dust Suppression in Underground Coal Mines. *Arabian J. Sci. Eng.* **2014**, *39*, 8319−8330.
(39) Zhu, X.; Wang, D.; Xu, C.; Zhu, Y.; Zhou, W.; He, F. Structure influence on jet pump operating limits. *Chem. Eng. Sci.* **2018**, *192*, 143−160.

https://doi.org/10.1021/acsomega.2c00684
ACS Omega 2022, 7, 12255−12267